JM3 Journal of Micro/Nanopatterning, Materials, and Metrology

RESEARCH PAPER

Indium nitrate hydrate films as potential EUV resists: film formation, characterization, and solubility switch assessment using a 92-eV electron beam

Jesse L. Grayson,[a] Marisol Valdez,[b] Weijie Xu,[a] and Julia W. P. Hsu[a,*]

[a]University of Texas at Dallas, Department of Materials Science and Engineering, Richardson, Texas, United States

[b]University of Texas at Dallas, Department of Chemistry, Richardson, Texas, United States

ABSTRACT. Indium nitrate hydrate films are evaluated as potential extreme ultraviolet (EUV) resists. To study the feasibility of these indium nitrate-based sol–gel precursor films as an EUV resist, the uniformity and stability of these films are examined as a function of metal composition, precursor concentration, chemical sources, precursor dissolution time, solvent drying time, post-application bake conditions, and relative humidity during the deposition. A 0.1 M indium nitrate hydrate solution forms a 20-nm thick resist, which is ideal for EUV lithography. We find two types of defects: macroscale defects that are visible under an optical microscope and nanoscale defects that can only be detected using an atomic force microscope. Both types of defects are affected by humidity during spin coating, dissolution time, and water content in the solvent. Hence, they are likely due to undissolved or re-crystallized indium nitrate hydrate crystals. The spin-coated indium nitrate hydrate films show great stability with no changes in defect density for up to 3 weeks. Using a 92-eV electron beam as a proxy for the EUV source, exposed regions of the film become insoluble upon exposure, acting as a negative-tone resist. Results of *operando* Fourier-transform infrared spectroscopy and residual gas analysis during the exposure show that the solubility switch is accompanied by the decomposition of nitrate species and the release of water. These results demonstrate the potential of indium nitrate hydrate films as an effective inorganic EUV resist.

Keywords: inorganic extreme ultraviolet resists; electron beam; indium nitrate hydrate; sol–gel films; solubility switch

Paper 23078G received Oct. 16, 2023; revised Dec. 4, 2023; accepted Dec. 12, 2023; published Jan. 2, 2024.

1 Introduction

Extreme ultraviolet (EUV) lithography is the most advanced lithography that can produce 10-nm resolution while having the capability of high-volume manufacturing. EUV lithography uses photons of 13.5 nm wavelength; because of the high energy of the photons, the photon number density is much lower than the traditional deep ultraviolet (DUV) sources at the same dose (radiant energy density).[1] Chemically amplified resists (CARs) have been the workhorse photoresist for DUV. When using CARs in EUV lithography, they suffer from lack of sensitivity because carbon has a low EUV absorption cross-section.[2] The requirement of thin resists in

*Address all correspondence to Julia W. P. Hsu, jwhsu@utdallas.edu

EUV lithography further exacerbates the problem. One approach to improve CARs' performance in EUV is to add more photoacid generators in the resist,[3,4] which has limited success.

Inorganic resists, in particular metal oxides, which are not used in DUV lithography, are studied as potential EUV resists because elements such as metal elements have larger EUV absorption cross-sections than carbon.[2] Tin (Sn) has been targeted because it has one of the highest EUV cross-sections. The most advanced inorganic EUV resist is based on Sn-oxo compounds.[5–7] The spherical Sn-oxo cages are made of tin-oxide cores surrounded by organic ligands and are a form of sol–gel precursors.[6] Resists are formed by spin-coating the precursor solution onto wafers to form thin films. The Sn-oxo compounds were shown to be a negative resist after EUV exposure.[7] In addition to Sn, there has not been significant research on inorganic EUV resists containing other metal elements with high EUV absorption cross-sections.

In this paper, we investigate indium nitrate hydrate $(In(NO_3)_3 \cdot x(H_2O))$ as a potential EUV resist. Indium nitrate hydrate is chosen because of the high EUV absorption cross-section of indium, the low thermal decomposition temperatures of metal nitrates,[8] and the adaptation of combustion sol–gel synthesis.[9] The EUV absorption cross-section for indium is comparable to that of tin; therefore, it should be sensitive to EUV.[2] The lower thermal decomposition temperatures of metal nitrates indicate that less energy is required to convert the salt to indium oxide compared with traditional sol–gel precursors with ligands such as acetates.[8,9] In addition, unlike Sn-oxo, indium nitrate hydrate contains no carbon.

The thermal conversion of indium nitrate hydrate to indium oxide begins by releasing water that was bonded to the salt, followed by the decomposition of the nitrates to nitric acid and water. At higher temperatures, NO/NO_2 and oxygen are released, and indium hydroxide is formed. Condensation and densification are the last two stages of the conversion as indium hydroxide converts to indium oxide.[8,10,11] The decomposition temperature can be further lowered using a combustion sol–gel formulation, which includes a fuel and an oxidizer. The fuel raises the energy content of the reactants, hence requiring less external energy to overcome the barrier for the exothermic reaction.[9]

Ideal photoresists should be uniform over the entire wafer and contain no defects. In this paper, we examine the uniformity and stability of indium nitrate hydrate films made from combustion sol–gel precursor formulation by characterizing their macroscale and nanoscale defects as a function of metal elements, precursor concentration, dissolution time, water content in the solvent, humidity during deposition, chemical vendors, and post-application bake (PAB) conditions.

The energy of EUV photons is 92 eV.[12] The absorption of EUV photons results in ionizing inner-shell electrons in metal elements such as In or Sn, and the photoelectrons subsequently induce chemical changes that lead to a solubility switch.[12,13] Electron beams (E-beams) are often used to study the interaction between the resist and EUV-generated photoelectrons.[12,14] The 92-eV E-beam has also been used as a proxy for the EUV source because EUV lithography systems are extremely expensive.[13,15,16] Although both EUV and E-beam of the same energy can produce a solubility switch, the dose required is not easily transferable between the two methods.[17] An additional difference is the absence of thermal processes in the EUV irradiation.[13,15] In this work, we test the solubility switch of indium nitrate hydrate films under a 92-eV E-beam exposure.

2 Methods

2.1 Indium Nitrate Hydrate Solutions

The indium nitrate resist formulation was adapted from Ref. 9. Indium(III) nitrate hydrate $(In(NO_3)_3 \cdot x(H_2O))$ was purchased from Sigma-Aldrich (#254215) and ThermoFisher Scientific (#010708). Most results in this report were taken using Sigma-Aldrich materials unless otherwise specified. Zinc nitrate hexahydrate (#96482) was purchased from Sigma-Aldrich. Tin(II) chloride hydrate was purchased from Alfa Aesar (#10894). Other reagents and solvents were purchased from Sigma-Aldrich unless otherwise specified, and everything was used as received. The preparation of the 0.1 M indium nitrate hydrate precursor solution begins by dissolving 141 mg $In(NO_3)_3 \bullet xH_2O$ in 4 mL of 2-methoxyethanol (2-MOE) solvent with continuous stirring. Once the metal salt is dissolved according to visual inspection, typically 1 h unless

otherwise specified, 40 μL of acetylacetone and 27 μL 14.5 M aqueous NH_3 are added, and the solution is allowed to stir overnight (12 h). To make the 0.1 M indium zinc oxide (IZO) precursor solution, we dissolve by stirring 75.8 mg $Zn(NO_3)_2 \bullet 6H_2O$ in 4 mL 2-MOE for 1 h, then add 40 μL of acetylacetone and 27 μL 14.5 M aqueous NH_3, and let the combined solution stir overnight (12 h). The IZO precursor is formed by mixing the In- and Zn-containing solutions in a 7:3 ratio and letting it stir for an additional hour. To prepare the 0.1 M indium tin oxide (ITO) precursor, 75.8 mg $SnCl_2$ with 32.02 mg NH_4NO_3 are added into 4 mL of 2-MOE and stirred for 1 h before adding 40 μL of acetylacetone and 13.5 μL of 14.5 M aqueous NH_3 and letting it stir for 12 h. The ITO precursor is formed by mixing the In- and Sn-containing solutions in a 9:1 ratio and letting it stir for an additional hour. For higher-concentration precursor solutions, the amounts were adjusted accordingly, and the same procedure was followed. All resist solutions are filtered with a 0.22 μm PTFE filter immediately before use.

To reduce the water content in the 2-MOE (drying 2-MOE), we first activated molecular sieves (3A Zeolite) by heating them in an oven for 48 h at 110°C. Then, the activated molecular sieves were put in a glass bottle and 2-MOE of three times the volume was added to it, which were allowed to sit for various periods of time. The dried 2-MOE was then used to dissolve indium nitrate hydrate as described above.

2.2 Resist Film Formation

The indium nitrate hydrate and IZO precursor solutions were spin-coated onto single- or double-sided polished (100) or (111) silicon wafer pieces cut to 1.5×3.8 cm^2 at a rate of 3500 rpm for 35 s. The ITO precursor was spin-coated onto the same substrates but at a rate of 2000 rpm for 35 s. Unless specified, all films are treated with PAB condition of 80°C for 3 min immediately following spin-coating.

2.3 Materials and Film Characterization

The spin-coated precursor films were studied using a Leica DM2500 M optical microscope equipped with a DFC450 microscope camera. For a quantitative analysis of the film quality, a defect density in units of #/mm^2 is calculated by processing images captured from the camera with ImageJ, a Java-based software developed by the National Institutes of Health in part with the Laboratory for Optical and Computational Instrumentation. Film roughness and nanoscale defects were studied using an atomic force microscope (AFM, Asylum Research MFP-3D) operating in tapping mode.

To evaluate whether the precursor films have been converted to oxides, we submerged the coated sample into a weak-acid developer solution composed of a 15:5:1 ratio of methanol, water, and acetic acid for 15 s to 1 min. Unconverted precursor films will be removed entirely from the substrate. Converted films that have undergone a solubility switch can no longer be removed by the developer.

The amount of water in the indium nitrate hydrate starting materials was characterized using thermogravimetric analysis (TGA) and differential scanning calorimetry (DSC) (Q600, TA Instruments) with a heating rate of 10°C min^{-1} from room temperature to 500°C. All experiments were conducted in air using as-received indium nitrate hydrate materials. The scanning electron microscopy (SEM) image is taken by a Zeiss Sigma 500VP SEM. The accelerating voltage is 3 kV.

2.4 Electron Beam Exposure

The E-beam system is described in Ref. 15. The electron gun (Kimbell physics, EGA-1012) is hosted in an ultrahigh vacuum (UHV) chamber (pressure $\sim 10^{-9}$ Torr) and can produce an electron beam with energy varying from 1 to 1000 eV. The E-beam impinges on the sample perpendicularly. During E-beam exposure, surface chemical changes can be monitored by *operando* infrared (IR) transmission measurement, and the released gases can be identified using a residual gas analyzer (RGA). The IR source and the MCT-B detector are located outside the chamber. The chamber has KBr windows for the IR beam to pass through. The sample is positioned at the Brewster angle with the IR beam. All IR spectra were measured with a resolution of 4 cm^{-1}, and the spectral range was 400 to 4000 cm^{-1}. The RGA was inserted from the top side of the

UHV chamber. In addition, the sample can be heated up to 1000 K through resistive heating, enabling us to compare thermal versus E-beam stimulated conversion.

The Si wafer coated with indium nitrate hydrate resist was held on the sample holder by two metal clips on both sides. The clips ensure that the sample does not move during loading, unloading, or the experiment. A metal mask was taped onto the wafer with copper tape to create exposed and unexposed regions on the resist. The sample holder is placed into a load lock chamber and pumped down to 10^{-9} Torr. Once the pressure is stable, the sample is transferred to the sample holder in the experimental chamber. The sample is rotated to the Brewster angle for the FTIR measurement and kept in place throughout the E-beam experiment. This ensures a constant FTIR intensity.

The E-beam energy and dose have been calibrated using a Faraday cup. When calibrating the energy, the cover on the Faraday cup was biased using a power supply while measuring the current using an ammeter. As the voltage of the Faraday cup is increased to 92 V, the electrons are repelled, and the current decreases abruptly. The E-beam energy is the value of the voltage at the intercept between the linear extrapolation of the current density and the background. The dose was determined from the Faraday current density at a given energy and emission current.

3 Results and Discussion

3.1 Macroscale Defects

The indium nitrate hydrate resist films in this research exhibit small circular defects visible under an optical microscope, as shown in Fig. 1(a). The defects are comprised of a nonhomogeneous feature surrounded by a halo that has a different optical contrast, possibly due to different thicknesses. When viewed at a higher magnification in SEM, the crystalline structure becomes apparent [Fig. 1(b)]. These are likely indium nitrate hydrate crystals arising from incomplete dissolution. Most results in the report were based on a 1-h indium nitrate hydrate dissolution time unless otherwise specified. The effect of dissolving time on film defects and morphology is discussed in Sec. 3.8. The following section characterizes these macroscale defects as a function of humidity, precursor concentration, metal elements, and PAB conditions.

3.2 Effects of Metal Cations

We next explore mixed cations to minimize crystallization in indium nitrate hydrate precursor films when exposed to air, moisture, or over an extended period.[18] In particular, the addition of zinc or tin to make ITO or IZO is well documented, and both have myriad applications as transparent conducting oxide thin films.[9,11,18]

The effects of adding zinc or tin to form mixed cation sol–gel precursor films are shown in Fig. 2. As shown in Fig. 2(b), ITO precursor films developed large, dendritic crystals, which were not seen in other precursor films within the timeframe of the experiment. Unlike the indium nitrate hydrate films that show circular dot defects [Fig. 2(a)], IZO precursor films exhibit

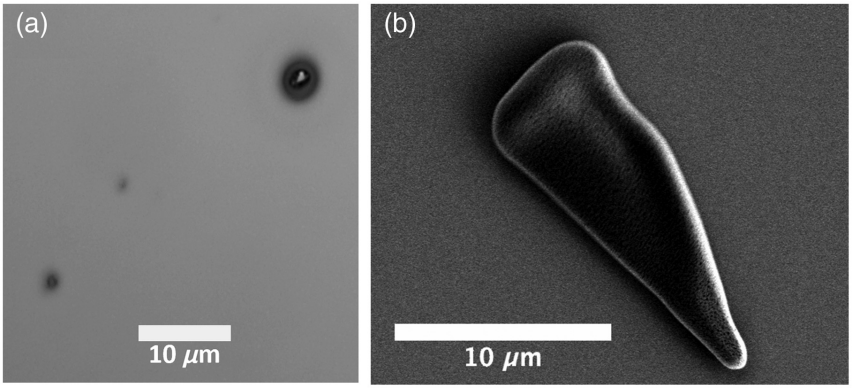

Fig. 1 (a) An optical microscope image showing macroscale defects of different sizes on a 0.1 M indium nitrate hydrate film and (b) a close-up SEM image of a macroscale defect. The sample was made at RH = 23% using the ThermoFisher material.

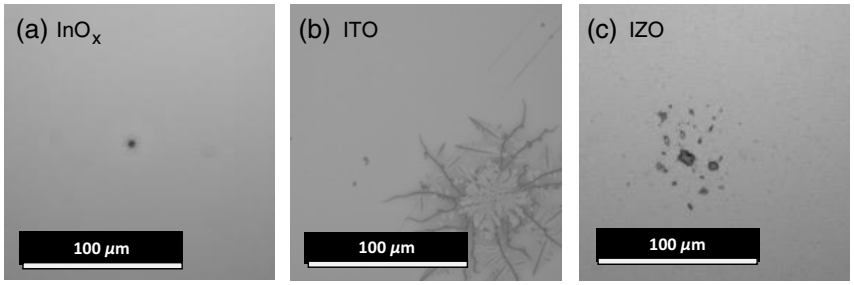

Fig. 2 Comparison of macroscale defects and non-uniformity observed on (a) indium nitrate hydrate, (b) ITO, and (c) IZO precursor films. All films were made from 0.1 M solutions at RH = 35%.

irregularly shaped zinc-rich clusters [Fig. 2(c)]. Overall, the indium nitrate hydrate precursor films are the most uniform.

3.3 Concentration Dependence

It is well known from solution chemistry and sol–gel science that the concentration can drastically impact the stability of a solution as well as the physical properties of a film after deposition.[19] As the ratio between solute and solvent increases, the potential for interactions between particles in a colloidal system increases. Higher concentration solutions typically have poor solution dispersion, poor stability, and suffer agglomeration of particles. These concentration effects can carry into the formation of the thin film after deposition.

In this study, the molarity of indium nitrate hydrate sol–gel precursor was varied between 0.1 and 0.4 M to ascertain the optimal concentration for film formation. Each of the four concentrations was prepared following the procedure described in Sec. 2.1. The simplest method of evaluating the film qualitatively is by eye and analysis under an optical microscope to see the macroscale defects.

Figures 3(a)–3(d) show examples of optical microscope images taken of indium nitrate hydrate precursor films. As the concentration increases, the defects begin to cover a larger portion of the film. The small dots on 0.1 M films in Fig. 1(a) develop large circular void regions around them when the concentration is increased to 0.3 M and 0.4 M, as shown in Figs. 3(c) and 3(d). Comparing the defect density for films made with different concentration precursors [Fig. 3(e)] reveals that high-concentration films have greater defect densities than low-concentration films. Ideal photoresists should have little to no defects; therefore, the indium nitrate hydrate sol–gel precursor should be 0.2 M or below. For the rest of the proceedings, we focus on 0.1M indium nitrate hydrate films.

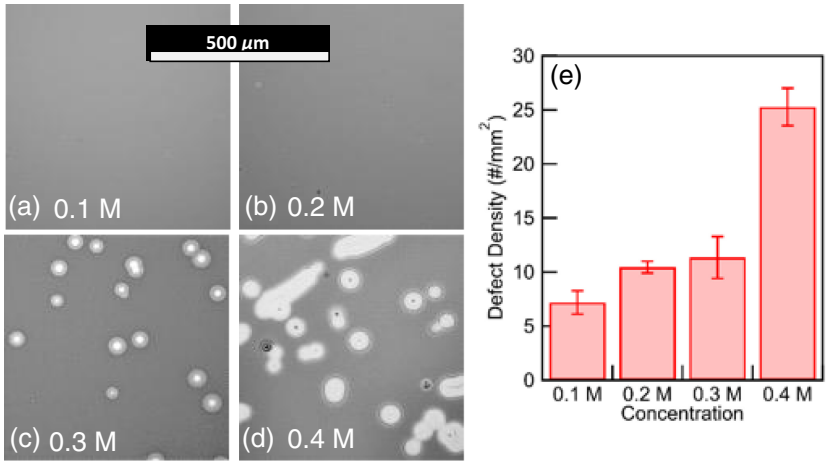

Fig. 3 Examples of optical microscope images from (a) 0.1 M, (b) 0.2 M, (c) 0.3 M, and (d) 0.4 M indium nitrate hydrate films, all made at RH = 26%. (e) The effect of precursor concentration on macroscale defect density.

3.4 Humidity Effect and Film Aging

Humidity is well known to affect sol–gel film formation, especially for hydrous metal oxides during the precursor solution and drying stages.[20,21] In an industrial fab, environmental conditions such as temperature and humidity are rigorously regulated. However, in an academic research laboratory, the ambient environment is not controlled. Winter days typically have a low relative humidity (RH), whereas summer days have a high RH value. This research on indium nitrate hydrate film formation and stability was subject to drastically varying relative humidity depending on the weather and the time of the year. We determine the macroscale defect density by counting the number of defects described in Sec. 3.1 from an optical microscope image using ImageJ then dividing by the area of the image. The humidity value is taken from a VWR traceable digital humidity temperature/dew point meter (#89500-398) placed inside the fume hood where the indium nitrate hydrate films are spin-coated. The year-long investigation of film defect density as a function of RH varying from 26% to 50% is shown in Fig. 4(a). At low (<29%) and high (>46%) RH, the films have a lower defect density but are subject to other non-uniformities. When the humidity is very low, the films can be impacted by the formation of dendritic crystals over time. When the humidity is high, the resist films develop the nanoscale features characterized in Sec. 3.5. Over the moderate humidity level range of 30% to 45% RH, the defect density is approximately independent of relative humidity, and the films are less impacted by crystal growth and nanoscale features. In the semiconductor manufacturing industry, a common RH range is (45 ± 5%).[22] Thus, our experiments covered the working conditions to which the indium nitrate hydrate photoresist will likely be exposed in an industrial setting. In Sec. 3.8, we show that the defect density depends on the dissolution time and can be further decreased at a given humidity.

Another important factor to consider is how these defect features change over time. Ideally, the time between photoresist application, PAB, and EUV exposure should be kept as short as possible; however, a resist should still exhibit excellent stability over the total processing time. This requires the resist not to develop new defects over time. To determine the stability of indium nitrate hydrate films, the defect density of a 0.1 M indium nitrate hydrate sol–gel precursor film

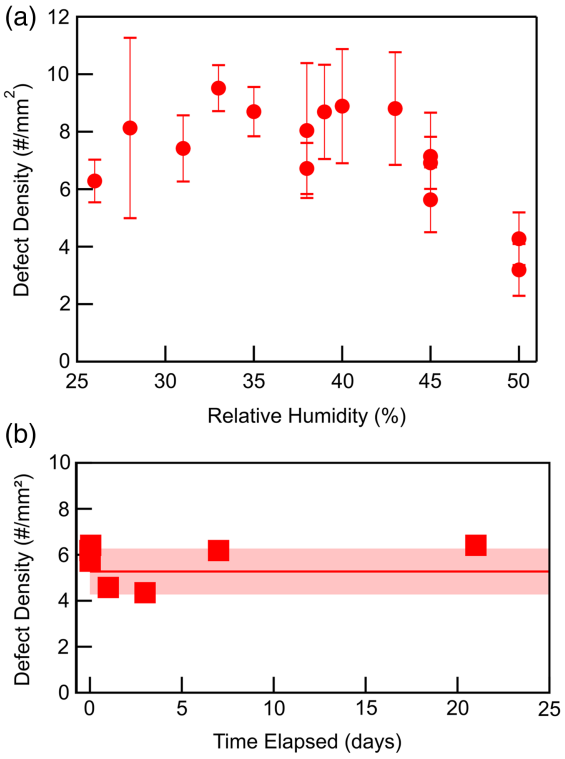

Fig. 4 (a) The effect of RH on macroscale defect density of 0.1 M indium nitrate hydrate films and (b) the stability of macroscale defect density on a 0.1 M indium nitrate hydrate film made at RH = 39% versus time elapsed after PAB (80°C for 3 min).

made at RH = 39% was monitored for an extended period after PAB using an optical microscope. Figure 4(b) shows that, even for 20 days after PAB, the film manifested no crystallization or change in defect density. Other films were monitored for shorter times but also showed no new defects. The fact that these films were kept in an ambient environment and faced variation in humidity after the initial application step demonstrates the stability of the indium nitrate hydrate sol-gel precursor film.

3.5 Nanoscale Defects

In addition to the macroscale defects that can be seen under an optical microscope, AFM scans revealed nanoscale "bump" features [Fig. 5(a) inset] in some of the indium nitrate hydrate films. They appear to be clusters of small crystals, most likely indium nitrate hydrate salt, clearly apparent from the AFM image of a single bump [Fig. 5(b)]. Away from the bumps, the film is very smooth with root-mean-squared (RMS) roughness of (1.0 ± 0.1) nm over 1 μm $\times$ 1 μm areas. Although these bump features vary in height, diameter, and density, their overall appearance remains the same. The amount of material accumulated in these nanoscale bumps can be quantified by approximating the bumps as cylinders and calculating the volume density using the equation $\frac{\pi}{4}\mathrm{d}(\mu\mathrm{m})^2 * \mathrm{h}(\mathrm{nm}) * \rho(\frac{\#}{\mu\mathrm{m}^2})$, where d is the bump diameter, h is the height, and r is the areal density. The bump volume density as a function of RH from 20% to 50% is presented in Fig. 5(c), which displays an overall positive trend. Because these bumps only appear at high humidity [circles in Fig. 5(c)] and their volume density increases with RH, we postulate that moisture in the air induces the agglomeration of indium nitrate hydrate crystals in the sol–gel precursor solution or during the spin coating process. To support this hypothesis, we made a resist film in the morning when the RH was 40% and observed the nanoscale bumps. Then, later that same day when the RH had dropped to 27%, we made another film using the same precursor solution, spin-coating procedure, and PAB condition and found that the film had no bumps [Fig. 5(d)].

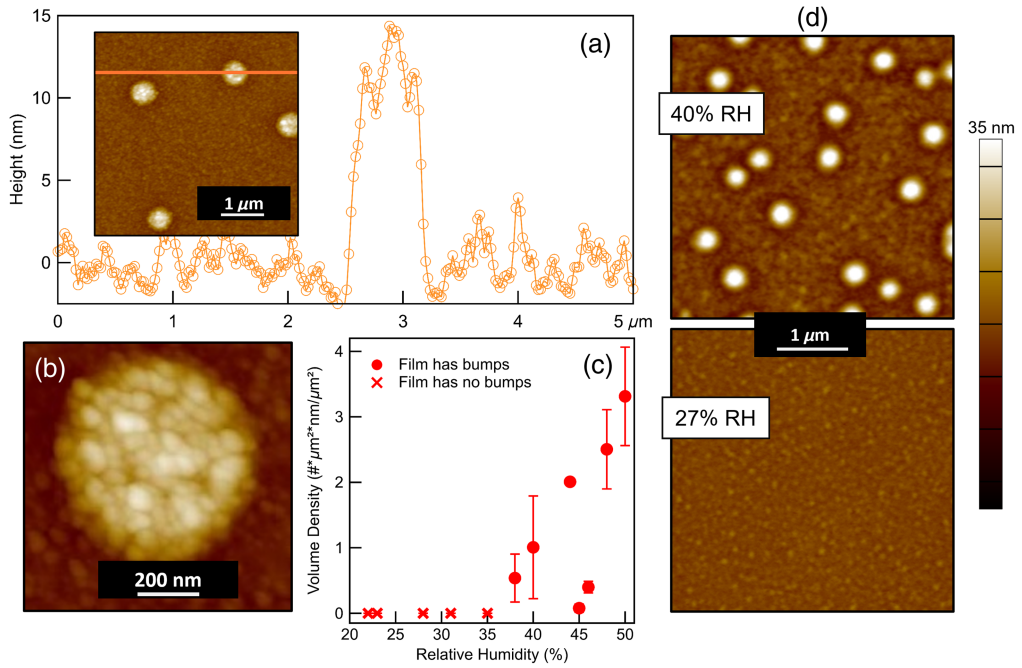

Fig. 5 (a) Topographic trace over one nanoscale bump on a 0.1 M indium nitrate hydrate film made at RH = 38%. Inset: An AFM image showing multiple nanoscale bumps. (b) A magnified image of one bump to show the internal structure. (c) The effect of RH on the volume density of these nanoscale bumps. Data points marked with an "x" indicate humidity levels at which no bumps appeared on the film. The PAB condition for films in (a)–(c) was 80°C for 3 min. (d) Two films were made using the same precursor solution on the same day: bumps are present when the RH = 40% and absent when RH = 27%. The PAB condition was 90°C for 2 min.

3.6 PAB Conditions

PAB is an important photolithography step: after spin-coating, the applied film is heated at a low temperature to remove excess solvent, stabilize the film, and enhance the sensitivity to exposure.[23] The PAB must be optimized in both time and temperature. A resist that undergoes a PAB condition too low in temperature or too short in time would require an excess exposure dose or continue to change before exposure. A bake that is too high in temperature or too long in time could result in thermal conversion of the entire resist, rendering patterning in the exposure step ineffective. The procedure in the previous experiments employed a PAB condition of 80°C for 3 min immediately following spin-coating. Taking 80°C as a starting point, we tested higher temperatures to evaporate as much 2-MOE as possible. Increasing temperature also means supplying the pre-exposed resist with more thermal energy that might lower the exposure dose required to induce photochemical reactions. The easiest method of testing other PAB conditions was to vary the PAB time at a given temperature until the precursor film could no longer be removed by the developer, i.e., thermally converted. Figure 6(a) shows all of the explored PAB conditions and resultant outcomes: green circles indicate that the film can still be removed by the developer and can be used for electron-beam or EUV exposure studies and red crosses indicate that the precursor film is already thermally converted and cannot be used as a resist. From the plot, it is clear that the bake time must be reduced at higher temperatures.

PAB conditions of 90°C for 2 min and 100°C for 1 min were chosen for further characterization to compare with 80°C for 3 min. The second column of Table 1 (Sigma-Aldrich material) reveals that the higher temperature baking results in a reduction in film thickness (i.e., more solvent was removed). Further comparisons of the macroscale defect density and volume density of nanoscale defects for the three PAB conditions are shown in Figs. 6(b) and 6(c), respectively. Figure 6(b) shows similar macroscale defect densities for the three PAB conditions. Figure 6(c) shows that nanoscale bump volume densities are similar for 80°C for 3 min and 90°C for 2 min and much lower for 100°C for 1 min. This might lead one to think that a PAB of 100°C for 1 min

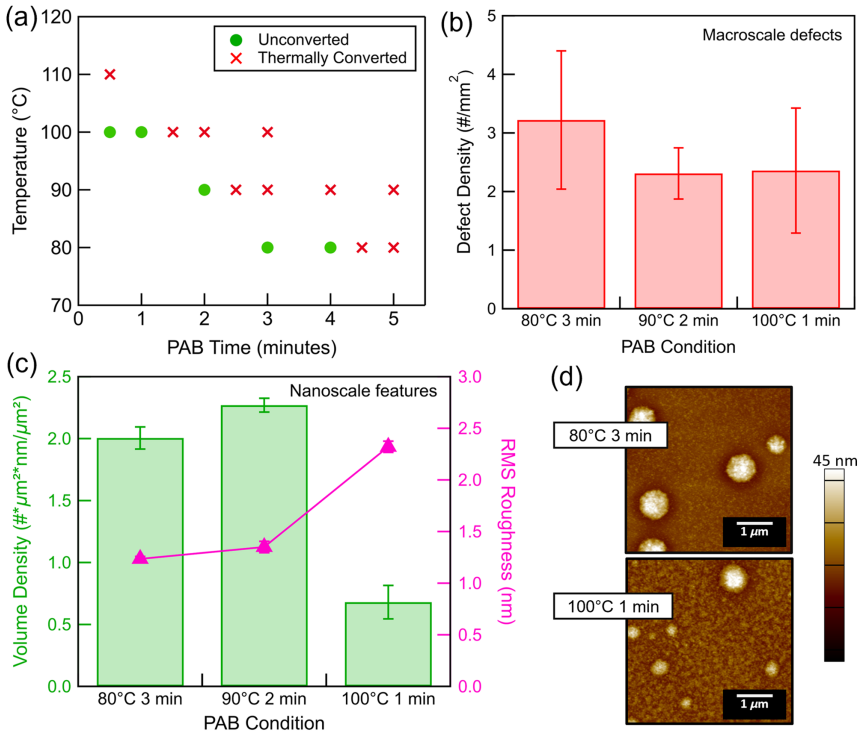

Fig. 6 (a) Outcomes of PAB as a function of temperature and time. (b) The effect of the PAB condition on macroscale defect density characterized with optical microscope and ImageJ. (c) The effect of the PAB condition on nanoscale feature volume density (left axis) and RMS roughness averaged from five 1×1 μm^2 areas (right axis) characterized with AFM. (d) AFM images of a film made with PAB condition of 80°C for 3 min (top) and film made with PAB of 100°C for 1 min (bottom). RH = 40% for films shown in (b) and (c) and 44% for the films shown in (d).

Table 1 Effect of the PAB condition on 0.1 M indium nitrate hydrate film thickness measured by ellipsometry.

PAB condition (RH = 44%)	Thickness (Sigma-Aldrich)	Thickness (ThermoFisher)
80°C for 3 min	31 ± 0.1 nm	33 ± 0.1 nm
90°C for 2 min	23 ± 0.1 nm	30 ± 0.1 nm
100°C for 1 min	22 ± 0.1 nm	29 ± 0.1 nm

would be better than lower temperatures. However, the 100°C PAB film has a much higher RMS roughness [pink triangles, the right axis in Fig. 6(c)]. Figure 6(d) clearly shows the effect of PAB on surface morphology. Films with rougher topography are undesirable for lithography. Choosing which PAB condition involves knowing the trade-offs and how they affect the overall resist performance.

3.7 Effects of Chemical Suppliers

For all of the above results except Fig. 1, the indium nitrate hydrate was purchased from Sigma-Aldrich. When seeking to order more chemicals, the only available supplier was ThermoFisher Scientific. The indium salts from the two vendors have different appearances: the Sigma-Aldrich indium nitrate hydrate materials are small semi-translucent crystals and dissolve quickly in 2-MOE, whereas the ThermoFisher materials are large opaque chunks and take much longer to dissolve. The following sections characterize their differences beyond appearance.

3.7.1 *Defect density and film morphology*

We prepared the precursor solution from the ThermoFisher indium nitrate hydrate as described in Sec. 2.1 but lengthened the precursor dissolution time from 1 h to 4 to 6 h to ensure that the salt was properly dissolved. We compare indium nitrate hydrate materials from the two vendors based on film defects while keeping the humidity and PAB conditions the same.

Figures 7(a) and 7(b) show pictures of the indium nitrate hydrate crystals from Sigma-Aldrich and ThermoFisher, respectively. The latter has a larger size. Their macroscale defect densities are similar [Fig. 7(c)], and their thicknesses are comparable at 20 to 30 nm (Table 1). However, unlike the Sigma-Aldrich films, ThermoFisher films did not show a substantial reduction in thickness with increasing PAB temperatures (rightmost column of Table 1). An even more drastic difference came from AFM analysis and the volume density of the nanoscale bumps. Figure 7(d) shows that ThermoFisher films have a 25% lower bump volume density, indicating that fewer indium nitrate hydrate crystals are in the aggregation and the film is more uniform. The largest contributor to this reduced nanoscale volume density is likely the increased dissolving time used for the ThermoFisher indium nitrate hydrate when making the precursor solutions. Figures 7(e) and 7(f) show AFM images taken on precursor films made from Sigma-Aldrich and ThermoFisher indium nitrate hydrate salts, respectively; the differences in the nanoscale surface morphology can be seen. Although the ThermoFisher films have a greater number of bumps, the bumps are smaller both in diameter and height. However, unlike Sigma-Aldrich films that develop nanoscale bump features only at RH $\geq$ 38%, we observed the presence of bumps on ThermoFisher films made at humidity levels at RH = 33%. Analysis of a ThermoFisher resist made at RH = 30% revealed no bumps, indicating that the minimum humidity level required to form nanoscale features on films using this chemical is likely between 30% and 33%. Although we only have data for ThermoFisher films at a few RH values below 44%, it also shows an increasing bump volume density with increasing the RH similar to the Sigma-Aldrich materials shown in Fig. 5(c).

3.7.2 *Thermal analysis*

Due to the difference in the time needed to dissolve the indium nitrate hydrate crystals, we postulate that there is a difference in their hydrate content, $In(NO_3)_3 \cdot x(H_2O)$. We used TGA and

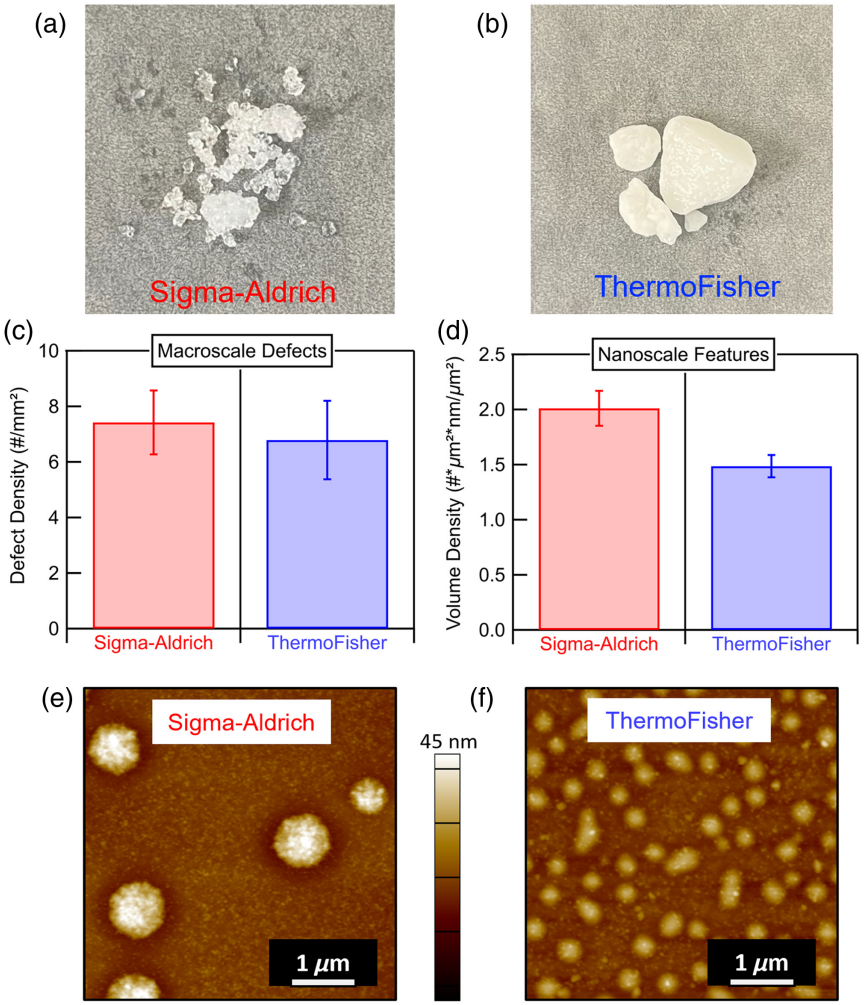

Fig. 7 Pictures of indium nitrate hydrate crystals procured from (a) Sigma-Aldrich and (b) ThermoFisher. Comparison of (c) macroscale defect density and (d) nanoscale feature volume density for films made from the two sources. AFM images of films made using (e) Sigma-Aldrich and (f) ThermoFisher indium nitrate hydrate. All films were made with a PAB of 80°C for 3 min and at RH = 44%.

DSC to investigate the possible difference in the materials from the two chemical suppliers (Fig. 7). TGA shows 39.8% of the mass left at high temperatures for the Sigma-Aldrich material [Fig. 8(a)] and 41.1% mass left for the ThermoFisher material [Fig. 8(b)]. Assuming only inorganic materials remain at high temperatures, the leftover mass must be indium oxide, In_2O_3. Thus, we can calculate the water content in the indium nitrate hydrate: $x_{\text{Sigma-Aldrich}} = 2.7$ and $x_{\text{ThermoFisher}} = 2.0$. Using the weight loss from room temperature to 150°C and assuming it is entirely due to the loss of water in the indium nitrate hydrate, we obtain $x_{\text{Sigma-Aldrich}} = 2.3$ and $x_{\text{ThermoFisher}} = 1.3$. Therefore, the Sigma-Aldrich indium nitrate hydrate contains more water. Because nanoscale bumps are linked to the humidity and metal salt dissolution time, the TGA results agree with the bump density results shown in Fig. 7 that Sigma-Aldrich films contain more materials in the aggregation form and that the lower water content requires more time to properly dissolve, as we investigate in Sec. 3.8. For the DSC, the endothermic peaks are 79°C, 180°C, and 206°C for the Sigma-Aldrich material and 74°C, 150°C, and 195°C for the ThermoFisher materials. The peaks at 74°C to 79°C can be attributed to the evaporation of water. The 150°C to 180°C peak can be identified with the loss of HNO_3 and 195°C to 206°C is the conversion of In-OH to indium oxide.[8]

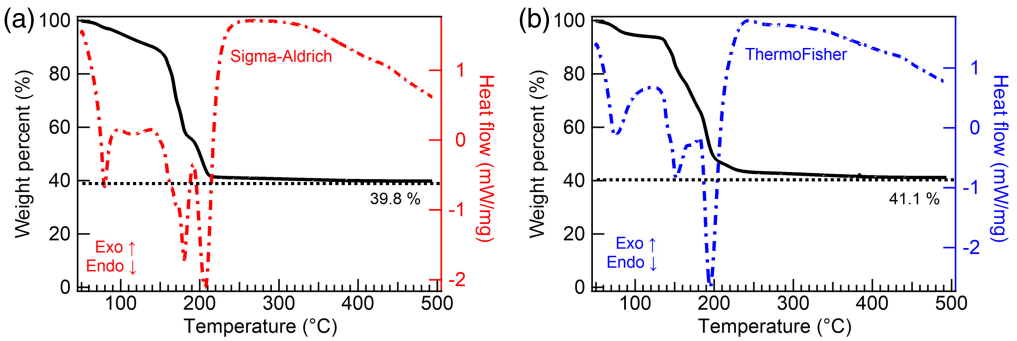

Fig. 8 TGA (black curves, left axis) and DSC (color curves, right axis) results for as-received indium nitrate hydrate from (a) Sigma-Aldrich and (b) ThermoFisher. The weight percentages of the starting materials that remained at high temperatures are indicated in the graphs.

3.8 Dissolution Time on Nanoscale Defects and Film Roughness

When preparing precursor solutions, a certain amount of time must be allowed for the solute to dissolve or the components to mix. As mentioned in Sec. 3.1, the defects that we observe on our resist films are likely indium nitrate hydrate crystals arising from incomplete dissolution. To test this conjecture, we compare defects in films made from dissolving the indium nitrate salt in 2-MOE overnight instead of for only 1 h, our previously established protocol as stated in Sec. 2.1. Precursor solutions prepared overnight produce films that are more uniform with fewer macroscale defects at low humidity, but the difference disappears at high humidity. At an RH of 23%, a longer dissolution time results in a 4× lower macroscale defect density, and both produce a low defect density at RH = 40% [Fig. 9(a)]. However, despite not observing an impact on the macroscale defects at 40% RH, AFM analysis reveals that the longer dissolution reduces the RMS

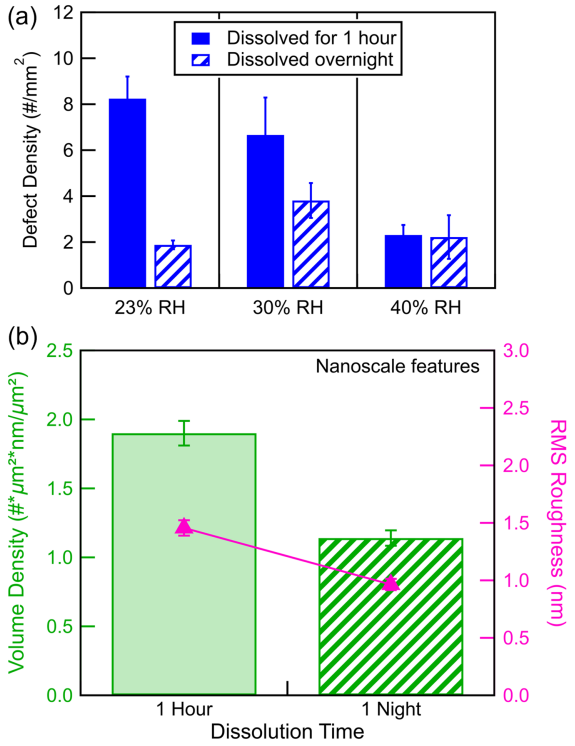

Fig. 9 (a) Comparison of macroscopic defect density of films made at three RHs with indium nitrate hydrate dissolved for 1 h (solid) versus overnight (hatched) in 2-MOE before adding reagents. (b) Comparison of volume density and surface roughness of a film made using a precursor solution with 1-h dissolution versus overnight dissolution, both samples made at RH = 40%. PAB condition for all films was 90°C for 2 min.

roughness and volume density of nanoscale features [Fig. 9(b)]. Overall, allowing the indium nitrate hydrate to dissolve for at least overnight improves the film quality and will be adopted into our precursor solution preparation going forward.

3.9 Removing Water from Solvent

We postulate that both the macroscale and nanoscale defects are caused by undissolved or re-crystallized indium nitrate hydrate crystals because the problems were lessened with a longer dissolution time and exacerbated when the humidity was higher. Because the solvent is an alcohol, it can uptake water from the environment over time, promoting crystallization. Therefore, we dried the 2-MOE solvent using molecular sieves before using it to dissolve indium nitrate hydrate crystals. The length of time allowed for the molecular sieves to uptake water from the starting solvent was varied from 2 to 19 days before preparing precursor solutions as described in Sec. 2. Samples made from dissolving indium nitrate hydrate in regular (un-dried) 2-MOE at the same time are used for comparison. We found that the macroscale defect density decreases compared to the control when the sieve-dried 2-MOE was used for all drying times [Fig. 10(a)]. The nanoscale bump volume density also decreases when the resist solution is made with dried 2-MOE, but it shows a clear dependence on drying times. The nanoscale defect volume density decreases by roughly half after 2 days of drying, down to about 10% after 15 days of drying, and becomes completely absent after 19 days of drying [Fig. 10(b) left axis]. These results agree with the humidity dependence of macroscale and nanoscale defects: macroscale defects are not sensitive to humidity [Fig. 4(a)], whereas nanoscale defects have a strong humidity dependence [Fig. 5(c)]. By contrast, the roughness away from the nanoscale bumps remains unchanged with drying times and is comparable to the roughness of the resist made with the un-dried solvent [Fig. 10(b) right axis].

3.10 Electron Beam Conversion Results

We expose indium nitrate hydrate precursor films to a 92-eV E-beam at an emission current of 0.6 mA through a mask to evaluate the differences between exposed and unexposed regions. Figure 11 shows the results of a sample undergoing E-beam exposure for 10 min, with an exposure dose of 8.0 mC/cm^2. The PAB condition was 80°C for 3 min. The operando time-sequence FTIR results [Fig. 11(a)] show a major loss of water (~3500 cm^{-1}) and ammonia (~3200 cm^{-1}) within the first 2 min of exposure.[8] As the exposure continued, the loss of nitrate and nitrite shown by the N-O vibration mode (~1550 to 1250 cm^{-1}) proceeded until the 8 min of exposure.[8,11] We confirm the identities of evolved gas molecules using RGA simultaneously. Figure 11(b) shows the operando RGA mass spectrum. By comparing with the NIST WebBook,[24] the gases released from the sample during the E-beam exposure are H_2O—the strongest intensities occur at $m/z = 17$ (17%) and 18 (81%), NH_3—$m/z = 16$ (42%) and 17 (52.5%), and NO—$m/z = 30$ (89%). These results are consistent with the molecular peak

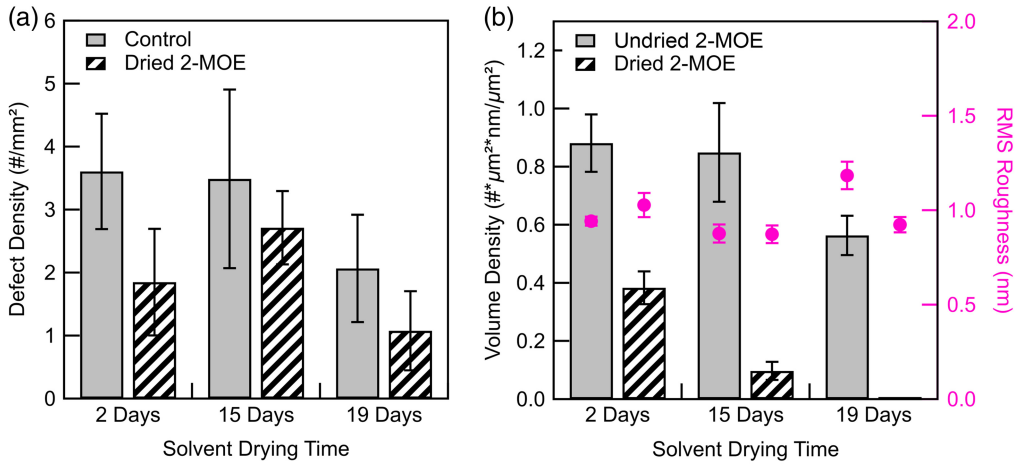

Fig. 10 Effects of solvent drying time on (a) macroscale defects and (b) nanoscale defects and film roughness. All films made at an RH value between 44% and 45%.

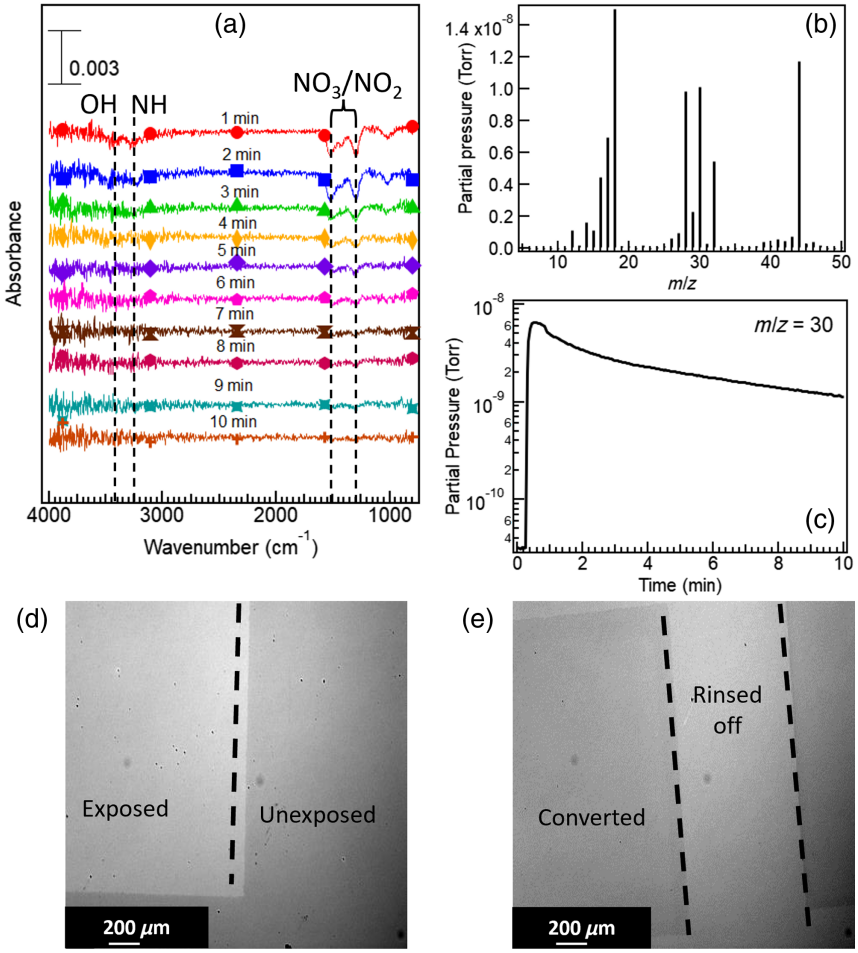

Fig. 11 (a) *Operando* FTIR spectra as a function of E-beam exposure time: 1 min (red circles), 2 min (blue squares), 3 min (green triangles), 4 min (yellow diamonds), 5 min (purple rotated squares), 6 min (magenta pentagons), 7 min (brown hourglasses), 8 min (crimson hexagons), 9 min (teal stars), and 10 min (burnt orange crosses). (b) RGA mass spectrum of E-beam exposed indium nitrate hydrate (Sigma-Aldrich) film made with the PAB condition of 80°C for 3 min. The E-beam exposure was performed at a beam voltage of 92 eV with an emission current of 0.6 mA for 10 min duration, resulting in a total dose of 8 mC/cm^2. (c) RGA loss of NO ($m/z = 30$) versus exposure time shows integrated partial pressure of 2.3×10^{-8} (Torr*min). Optical images show visual changes of the masked resist film (d) after exposure before development and (e) after development. The unexposed areas are removed by the developer.

losses detected by FTIR in Fig. 11(a). The signals observed at $m/z = 28$, 32, and 44 are from background N_2, O_2, and CO_2, respectively, in the chamber, but their partial pressures are 1×10^{-9} Torr or below. The time evolution of NO release ($m/z = 30$) is shown in Fig. 11(c) with the integrated partial pressure calculated to be 2.3×10^{-8} Torr $*$ min. After the exposure, the contrast between the exposed and unexposed regions was visible by the eye and under an optical microscope [Fig. 11(d)]. The solubility switch is demonstrated by developing the exposed sample in a weak acid [Fig. 11(e)]: the weak acid developer rinsed off the unexposed regions, whereas the exposed areas were insoluble and stayed on the silicon. We also performed E-beam exposure experiments with indium nitrate hydrate samples processed with PAB conditions of 90° C for 2 min and 100°C for 1 min and found similar results.

4 Conclusion

We investigated the uniformity and stability of indium nitrate hydrate sol–gel precursor films as potential EUV resists. Varying the precursor concentrations and mixed cations indicated that

films made from 0.1 M pure indium nitrate hydrate were the most uniform and stable over time in a standard laboratory environment. These films were about 20 to 30 nm thick post PAB, making them suitable as EUV resists. Quantitative analyses of optical microscopy and AFM images were performed to characterize defects at both the macroscale and nanoscale. We found that relative humidity, precursor dissolution time, and water content in the 2-MOE solvent have a large effect on film morphology and defect density, particularly regarding the nanoscale defects, but that PAB has a small impact. In addition, we found that precursor materials procured from different vendors have a different appearance and water content; they produce films with different morphology and nanoscale defects. The E-beam exposure experiment successfully demonstrated the solubility switch in these indium nitrate hydrate films. The indium nitrate hydrate films behave as a negative resist with exposed areas remaining on the substrate and unexposed areas removed by the developer. *Operando* FTIR showed the loss of water, ammonia, and nitrate/nitrate within the first 10 min of exposure, which were confirmed by the RGA results. In summary, we established deposition and PAB conditions to fabricate uniform and stable indium nitrate hydrate films of a desired thickness for EUV lithography and demonstrated their sensitivity to solubility switch induced by 92-eV E-beam exposure. These results demonstrate the potential of indium nitrate hydrate films as an effective inorganic EUV resist.

Code and Data Availability

Data are available from the corresponding author upon request.

Acknowledgments

The authors acknowledge help from J. Bonner for ellipsometry measurements and analysis and M. Herrara for figure preparation. The authors also thank J. Blackwell, K. Tapily, and R. Burns for helpful discussions. The earlier version of this paper was previously published as an SPIE Proceedings paper in Ref. 25. This research was supported by the Semiconductor Research Cooperation (SRC) through the Nanomanufacturing Materials and Processes (NMP) Program (task# 3082). J. W. P. Hsu acknowledges the support of the Texas Instruments Distinguished Chair in Nanoelectronics.

References

1. R. Fallica et al., "Dynamic absorption coefficients of chemically amplified resists and nonchemically amplified resists at extreme ultraviolet," *J. Micro/Nanolithogr. MEMS MOEMS* **15**(3), 033506 (2016).
2. R. Fallica et al., "Absorption coefficient of metal-containing photoresists in the extreme ultraviolet," *J. Micro/Nanolithogr. MEMS MOEMS* **17**(2), 023505 (2018).
3. K. Okamoto et al., "Study on deprotonation from radiation-induced ionized acrylate polymers including acid-generation promoters for improving chemically amplified resists," *Jpn. J. Appl. Phys.* **61**(6), 066505 (2022).
4. S. Fujii et al., "Sensitivity enhancement of chemically amplified EUV resists by adding acid-generating promoters," *Jpn. J. Appl. Phys.* **56**(6S1), 06GD01 (2017).
5. J. Haitjema et al., "Extreme ultraviolet patterning of tin-oxo cages," *J. Micro/Nanolithogr. MEMS MOEMS* **16**(3), 033510 (2017).
6. Y. Zhang et al., "Photochemical conversion of tin-oxo cage compounds studied using hard x-ray photoelectron spectroscopy," *J. Micro/Nanolithogr. MEMS MOEMS* **16**(2), 023510 (2017).
7. B. Cardineau et al., "EUV resists based on tin-oxo clusters," *Proc. SPIE* **9051**, 90511B (2014).
8. E. A. Cochran et al., "Unique chemistries of metal-nitrate precursors to form metal-oxide thin films from solution: materials for electronic and energy applications," *J. Mater. Chem. A Mater.* **7**(42), 24124–24149 (2019).
9. M. G. Kim et al., "Low-temperature fabrication of high-performance metal oxide thin-film electronics via combustion processing," *Nat. Mater.* **10**(5), 382–388 (2011).
10. S. Park et al., "In-depth studies on rapid photochemical activation of various sol–gel metal oxide films for flexible transparent electronics," *Adv. Funct. Mater.* **25**(19), 2807–2815 (2015).
11. T. B. Daunis et al., "Solution-processed oxide thin film transistors on shape memory polymer enabled by photochemical self-patterning," *J. Mater. Res.* **33**(17), 2454–2462 (2018).
12. J. Torok et al., "Electron penetration depths in EUV photoresists," *J. Photopolym. Sci. Technol.* **27**(5), 611–615 (2014).

13. M. S. M. Saifullah, N. Tiwale, and R. Ganesan, "Review of metal-containing resists in electron beam lithography: perspectives for extreme ultraviolet patterning," *J. Micro/Nanopatterning, Mater. Metrol.* **21**(4), 041402 (2022).
14. M. Rohdenburg et al., "Role of low-energy electrons in the solubility switch of Zn-based oxocluster photoresist for extreme ultraviolet lithography," *Phys. Chem. Chem. Phys.* **23**(31), 16646–16657 (2021).
15. E. C. Mattson et al., "Chemical modification mechanisms in hybrid hafnium oxo-methacrylate nanocluster photoresists for extreme ultraviolet patterning," *Chem. Mater.* **30**(17), 6192–6206 (2018).
16. S. Bhattarai, A. R. Neureuther, and P. P. Naulleau, "Study of shot noise in photoresists for extreme ultraviolet lithography through comparative analysis of line edge roughness in electron beam and extreme ultraviolet lithography," *J. Vac. Sci. Technol. B Nanotechnol. Microelectron.* **35**(6), 061602 (2017).
17. Y. Zhang et al., "Dual-tone application of a tin-oxo cage photoresist under E-beam and EUV exposure," *J. Photopolym. Sci. Technol.* **31**(2), 249–255 (2018).
18. M. G. Kim et al., "High-performance solution-processed amorphous zinc-indium-tin oxide thin-film transistors," *J. Am. Chem. Soc.* **132**(30), 10352–10364 (2010).
19. C. J. Brinker and G. W. Scherer, *Sol-Gel Science: The Physics and Chemistry of Sol-Gel Processing*, Academic Press (2013).
20. Z. Su et al., "Effects of annealing temperature, ambient humidity and temperature on dielectric properties of sol–gel-derived amorphous alumina thin film," *J. Mater. Sci. - Mater. Electron.* **28**(16), 12356–12362 (2017).
21. H. Song et al., "Influence of humidity for preparing sol-gel ZnO layer: characterization and optimization for optoelectronic device applications," *Appl. Surf. Sci.* **512**, 145660 (2020).
22. Y. Zhao et al., "A comparative study on energy performance assessment for HVAC systems in high-tech fabs," *J. Build. Eng.* **39**, 102188 (2021).
23. C. Mack, *Fundamental Principles of Optical Lithography: The Science of Microfabrication*, pp. 199–209, John Wiley & Sons, Ltd. (2007).
24. "NIST chemistry WebBook," *Choice Rev. Online* **43**(12) (2006).
25. J. Grayson et al., "Indium nitrate hydrate films as EUV resists by evaluating with 92-eV electron beam," *Proc. SPIE, Advances in Patterning Materials and Processes XL*, **12498**, 170–184 (2023),

Jesse L. Grayson received her BS degree in electrical engineering and her MS degree in materials science and engineering from the University of Texas at Dallas in 2021 and 2023, respectively. Her primary research there focused on photoresists for application in EUV lithography. She is currently working at Applied Materials META Center located in Albany, New York.

Marisol Valdez is a research assistant in the Department of Materials Science and Engineering at the University of Texas at Dallas. She received her BS degree in chemistry and is currently in the PhD program in chemistry. Her research focuses on inorganic sol–gel materials for electron beam and EUV lithography applications.

Weijie Xu is a research assistant in the Department of Materials Science and Engineering at the University of Texas at Dallas. He received his PhD in materials science and engineering from the University of Texas at Dallas in 2023, where his research involves photo-irradiation based high-throughput fabrication of flexible oxide electronics and perovskite solar cells. He is currently working at Texas Instruments in Dallas, Texas.

Julia W. P. Hsu is a professor of materials science and engineering at the University of Texas at Dallas and holds the Texas Instruments Distinguished Chair in Nanoelectronics. She is a fellow of the American Physical Society, the American Association for the Advancement of Science, and the Materials Research Society. Her current research activities include novel materials and processing techniques for organic and perovskite solar cells, flexible electronics, and inorganic EUV resists.